A hybrid pore network-continuum modeling framework for flow and transport in 3D digital images of porous media

Li Zhang[a,b], Bo Guo[a,*], Chaozhong Qin[c,d], Yongqiang Xiong[b]

[a]*Department of Hydrology & Atmospheric Sciences, University of Arizona, Tucson, AZ, USA*
[b]*State Key Laboratory of Organic Geochemistry, Guangzhou Institute of Geochemistry, Chinese Academy of Science, Guangzhou, China*
[c]*State Key Laboratory of Coal Mine Disaster Dynamics and Control, Chongqing University, Chongqing, China*
[d]*School of Resources and Safety Engineering, Chongqing University, Chongqing, China*

Abstract

The presence of a wide range of pore sizes poses significant challenges for understanding flow and transport mechanisms in multiscale porous media (e.g., shale rocks, carbonates, tight sandstones, coalbed and soils). Recent advances in imaging technologies have provided high-resolution characterization of the multiscale pore structures. However, quantifying flow and transport in the 3D digital images requires models to represent both the resolved and sub-resolution pore structures. Here, we present a hybrid pore-network-continuum modeling framework to address this challenge. The hybrid framework treats the smaller pores (i.e., pores below the image resolution) as a continuum described by the Darcy equation and explicitly represents the flow and transport processes in the larger pores (i.e., pores that are resolved in the images) using a computationally efficient pore network model. We validate the new framework against direct numerical simulations based on the Darcy-Brinkman-Stokes framework for single-phase flow and solute transport. Our results suggest that the new hybrid model accurately predicts the overall flow and transport process and the mass transfer between the pore network and the sub-resolution microporous subdomains, while being much more computationally efficient than the direct numerical simulation methods. We then further demonstrate the applicability of the hybrid model for simulating two-component gas transport in shale rocks, i.e., the displacement of CH_4 by CO_2. The simulations illustrate the significant contribution of the continuum subdomain to the overall gas production. The developed h-PNM-continuum modeling framework may also be further extended to simulate more complex processes that involve multi-phase flow, reactive transport, and non-Newtonian displacement.

Keywords: Pore network model, Multiscale pore structure, Pore-scale model, 3D digital images, Hybrid modeling

*Corresponding author
Email address: boguo@arizona.edu (Bo Guo)

Key points:

1. We develop and validate a novel hybrid pore network-continuum modeling framework(h-PNM-continuum) for flow and transport in 3D multiscale pore structures.

2. The h-PNM-continuum model is accurate in modeling flow and transport and the mass transfer between the resolved-pore and continuum subdomains, while being much more computationally efficient than the DNS methods.

3. The h-PNM-continuum modeling framework can be extended for more complex processes involving multi-phase flow, reactive transport, and non-Newtonian displacement.

1. Introduction

Pore-scale flow and transport processes in porous materials play a critical role in many geoscience and engineering applications, such as hydrocarbon recovery, CO_2 sequestration, contaminant transport, nuclear waste storage, fuel cells, and biomedical applications. Thanks to advances in imaging technologies and computational modeling, pore-scale imaging and modeling (sometimes referred to as digital rock physics) have become a standard technology to study fluid flow and transport in porous media at microscopic scales (Blunt et al., 2013; Bultreys et al., 2016; Xiong et al., 2016). Advanced imaging and analysis techniques including non-destructive X-ray computed tomography (e.g., micro-CT or nano-CT), focused ion beam–scanning electron microscopy (FIB-SEM), transmission electron microscopy (TEM), and focused ion beam–helium ion microscope (FIB-HIM), have been increasingly used to visualize and quantify 3D pore-scale structures of porous media (Wildenschild & Sheppard, 2013; Cnudde & Boone, 2013). While imaging characterization can now achieve resolutions down to a few nanometers, digital images often cannot resolve all the pores of porous media with a wide range of pore sizes due to a trade-off between the spatial resolution and the size of the field of view. As a result, "two-scale" digital images—large pores resolved in the image and much smaller sub-resolution pores coexist—arise when applying imaging characterization to many porous media, e.g., shale rocks, carbonates, tight sandstones, coalbed, and soils. These unresolved microporous subdomains have been demonstrated to have a strong impact on the flow and transport processes for many applications, which suggests that they should be accounted for in modeling approaches (Mehmani & Prodanović, 2014; Bultreys et al., 2015; Scheibe et al., 2015; Soulaine et al., 2016; Mehmani et al., 2021).

The need to represent flow and transport processes in both scales of these two-scale images poses significant challenges to pore-scale modeling. Pore-scale modeling based on high-resolution images can be generally grouped into two categories(Meakin & Tartakovsky, 2009; Blunt et al., 2013; Xiong et al., 2016; Mehmani et al., 2021): (1) direct numerical simulation (DNS) and (2) pore network model (PNM). Both DNS and PNM approaches have been extended to model flow and transport in "two-scale" digital images. Soulaine & Tchelepi (2016) proposed a micro-continuum modeling framework based on the Darcy-Brinkman-Stokes equation (DBS), where the Stokes equation is solved in the resolved pores and Darcy's law is utilized for

the fluid flow in the sub-resolution microporous subdomain. The DBS framework has also been extended to include various additional processes, including solute transport (Scheibe et al., 2015), mineral dissolution and reactive transport (Golfier et al., 2002; Soulaine et al., 2017, 2018; Maes & Menke, 2021; You & Lee, 2021; Molins et al., 2021; Maes et al., 2022), gas and multi-fluid transport in shale rocks (Guo et al., 2018; Soulaine et al., 2019; Guo et al., 2019), two-phase flow (Carrillo et al., 2020; Maes & Menke, 2021; Carrillo et al., 2022), fluid-solid interaction and deformation (Carrillo & Bourg, 2019, 2021), and heat transfer (Maes & Menke, 2022; Xu et al., 2022). While the DBS-based micro-continuum model provides a DNS modeling framework for flow and transport in "two-scale" digital images, like any other DNS models, it requires high computation costs when simulating high-resolution digital images of porous materials.

PNM has also been extended in various forms to model the flow and transport processes in "two-scale" porous media. The extensions are often referred to as the dual pore network model (dual PNM). Bekri et al. (2005) presented a dual PNM that simulated mass transfer in a two-scale porous medium, which employed a large-scale network to represent vugs or fractures and a small-scale network for the homogeneous matrix. Bauer et al. (2012) introduces a dual PNM where the large-scale pore network is extracted from images, and micropores function as parallel throats alongside the resolved pore throats. Based on statistical information from the images at different scales, Jiang et al. (2013) employed stochastic methods to create a small-scale pore network, which then was combined with the larger-scale network, resulting in a two-scale network. Mehmani & Prodanović (2014) developed a dual PNM considering different connectivities between the big and small networks, and used the dual PNM to investigate the impact of microporosity on transport in porous media. Prodanović et al. (2015) extended this approach by determining the location of the small-scale pore network based on digital images of porous media samples. Bultreys et al. (2015) developed another dual PNM where the microporous regions are approximated as effective pore throats that can connect with the large-scale pore network in parallel and in serial. These methods generally require large computation costs due to a large number of network elements (if the pore structures in the microporous regions are explicitly represented) or greatly simply the spatial interconnectivity between the resolved pores and the microporous regions (when the microporous regions are approximated as effective throats).

To address the above-discussed challenges, we present a new hybrid pore network-continuum modeling framework (h-PNM-continuum). This hybrid framework treats the unresolved smaller pores (sub-resolution microporous regions) as a continuum described by the Darcy equation, while explicitly representing the flow and transport processes in the larger pores (the resolved pores) using a PNM. The pore network is extracted from the resolved pore subdomain using the watershed-segmentation-based SNOW algorithm developed by Gostick (2017). Additionally, we develop a new algorithm to connect the pore network to the microporous subdomain while extracting the pore network from the 3D image. Building upon the hybrid framework, we present mathematical formulations for single-phase flow, solute transport, and gas transport in nanoporous shale rocks that accounts for the confinement effects of gas flow in nanopores.

2. Hybrid pore network-continuum modeling framework (h-PNM-continuum)

In this section, we present the key ingredients of the hybrid modeling framework, which include a modified network extraction algorithm that links the extracted pore network to the microporous subdomain, mathematical formulations for single-phase flow, solute transport, and two-component gas transport in shale rocks, and numerical methods used to discretize and solve the governing equations.

2.1. Network extraction and coupling between the pore network and the microporous subdomain

For a ternary segmented image (image #1) that consists of three subdomains including resolved pores, sub-resolution microporous regions, and solids (Figure 1(a)), we need to extract the pore network from the resolved pore subdomain and then connect the pore bodies to the sub-resolution microporous subdomain based on original connectivity between the two subdomains. We do so by augmenting the watershed-segmentation-based SNOW algorithm developed by Gostick (2017). The augmented algorithm involves two steps: (1) decompose the ternary image to extract the pore network from the resolved pore subdomain (Figure 1(b1)) and discretize the continuum subdomain (Figure 1(b2)); and (2) couple the extracted pore network and the discretized microporous subdomain (Figure 1(c)). We present each step in the following subsections.

2.1.1. Network extraction and discretization

We decompose the ternary image (image #1) into two binary images (Figure 1): image #2 containing only the resolved pores and solid, and image #3 containing only microporous region (continuum) and solid. Then, we extract the pore network from image #2 using the watershed-segmentation-based SNOW algorithm developed by Gostick (2017) (Figure 1(b1)), where we approximate the pore bodies as spheres and pore throats as cylindrical tubes. The SNOW algorithm employs several techniques, including prefiltering the distance map, removing peaks on saddles and plateaus, and merging nearby peaks, to mitigate the peaks and the spurious local maxima resulting from over-segmentation of the standard watershed-segmentation-based algorithms (Rabbani et al., 2014; Gostick, 2017). When applying the SNOW algorithm, a multidimensional Gaussian blur filter with a sigma value of 0.35 is used to smooth the distance map. The radius of the structuring element in the maximum filter is set to 4. The network extraction algorithm provides the volume, coordination number, diameter, and surface area of each pore body, and the diameter, length, and connectivity of each pore throat. Finally, we discretize the microporous subdomain using structure grids (Figure 1(b2)). In the present work, the discretized numerical cells have a one-to-one correspondence to the voxels of the 3D digital image.

2.1.2. Coupling the pore network and the microporous subdomain

To couple the extracted pore network and the discretized microporous subdomain, we identify the voxels of the microporous subdomain residing at the boundary of each pore and subsequently link them to the corresponding extracted pore body. Taking pore i as an example, the coupling process involves the following

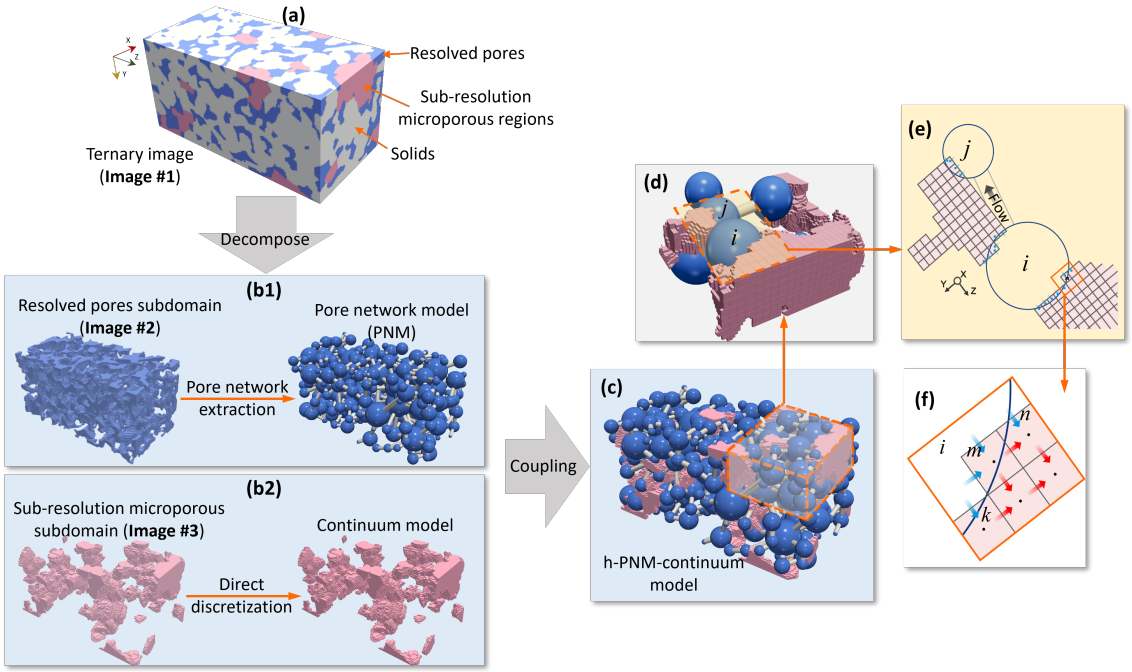

Figure 1: Schematic of the hybrid pore network-continuum modeling framework. (a) A ternary segmented image (Image #1) with blue, pink, and grey colors denoting the resolved pores, sub-resolution microporous regions, and non-porous solids, respectively. (b1) Pore network extraction from the resolved pore subdomain (Image #2). (b2) Numerical discretization of the sub-resolution microporous subdomain (Image #3). (c) The coupled hybrid pore network-continuum (h-PNM-continuum) representation of the original ternary image. (d) A zoom-in to illustrate the coupling between the pore network and the discretized continuum subdomain. (e) An example of pores i and j from (d) that are coupled with the discretized continuum subdomain. (f) A zoom-in of the interface between pore i and the adjacent numerical cells m, n, and k in the continuum subdomain.

morphological operations: (1) Dilate the watershed segment of pore i with a spherical structuring element of one-voxel radius. (2) Identify the interface voxels in the overlapping region of the dilated watershed segment of pore i and the microporous region surrounding this pore (we refer to these voxels as the interface voxels for this pore). For example, voxels labeled m, n, k in Figure 1(f) are the interface voxels for pore i. (3) Count the number of side faces of each interface voxel shared with pore i. This is done by dilating the interface voxel and counting the number of dilated voxels overlapped with pore i. (4) Append to pore i the information of its interface voxels, including the total number of interface voxels, the coordinates, and the number of shared faces of each coupled voxel. Using the above method, we identify the coupled voxels adjacent to each specific pore and finally couple the PNM and the continuum model. Note that the numerical grid cells of the continuum model have a one-to-one correspondence to the voxels in image #3. The extracted pore network and the coupling between the two submodels (Figure 1(c-f)) are then passed onto a computational framework to simulate flow and transport in two-scale digital images of pore structures.

2.2. Mathematical formulations

The hybrid pore-network-continuum modeling framework can used to model a wide variety of problems involving fluid flow and transport in two-scale porous media. In the present study, we focus on illustrating three example problems: (1) steady-state incompressible single-phase flow, (2) solute transport, and (3) two-component gas transport in shale. In the following subsections, we present the mathematical formulations for the three examples. Because of the small spatial scales involved, we do not consider gravity.

2.2.1. Steady-state incompressible single-phase flow

For steady-state incompressible single-phase flow, the mass balance equation in a pore body i of the resolved pore domain can be written as

$$\sum_{j=1}^{N_i} g_{ij}\left(p_i - p_j\right) + \sum_{m=1}^{M_i} q_{i,m} = 0, \tag{1}$$

where the subscript 'j' indicates the pore bodies adjacent to pore body i, and "m" indicates the grid cells in the continuum microporous subdomain that are connected to pore body i. "ij" indicates the pore throat between pore bodies i and j; "i,m" indicates the connection between pore body i and the connected continuum cell m. N_i is the number of pore bodies connected to pore body i (–). p_i and p_j are the pressure in pore bodies i and j, respectively (kg/m/s^2). $g_{ij} = \pi d_{ij}^4/(128\mu_{ij}l_{ij})$, is the conductance between pore bodies i and j (m$^4 \cdot$ s/kg), which is derived from Hagen-Poiseuille law for a bcylindrical tube. d_{ij} is the diameter of the pore throat ij (m), μ_{ij} is the gas viscosity (kg/m/s), and l_{ij} is the length of the pore throat ij (m). M_i is the number of continuum cells connected to pore body i (–). $q_{i,m} = k_{i,m}A_{i,m}\left(p_i - p_m\right)/(\mu_{i,m}l_{i,m})$ is the volumetric flux between pore body i and continuum cell m (m^3/s), where $A_{i,m}$ is the area of the interface (m^2), $l_{i,m}$ is the distance from pore body i to continuum cell m (m), and $k_{i,m}$ and $\mu_{i,m}$ are the permeability of the pore throat (m^2) and fluid viscosity (kg/m/s), respectively.

In the continuum microporous domain, the mass balance equation for a continuum cell m can be written as

$$\int_{\Omega_m} \nabla \cdot \left(-\frac{k}{\mu}\nabla p\right) dV + \sum_{i=1}^{W_i} q_{m,i} = 0, \tag{2}$$

where Ω_m denotes the domain of integration, i.e., the cell m. The subscripts "m,i" indicates the connection between the continuum cell m and the connected pore body i. k is the permeability of cell m (m^2). μ is the gas viscosity (kg/m/s). p is the pressure (kg/m/s^2). W_i is the number of pore bodies connected to continuum cell m (–). $q_{m,i} = k_{m,i}A_{m,i}\left(p_m - p_i\right)/(\mu_{m,i}l_{m,i})$ is the volumetric flux between continuum cell m and pore body i (m^3/s), where $A_{m,i}$ is the area of the interface (m^2), $l_{m,i}$ is the distance from continuum cell m to pore body i (m), and $k_{m,i}$ and $\mu_{m,i}$ are the permeability (m^2) and fluid viscosity (kg/m/s), respectively.

2.2.2. Solute transport

This section presents the governing equations for single-phase solute transport processes accounting for advection and dispersion.

For a pore body i, the solute conservation equation of a nonactive solute can be given as

$$\frac{\partial\left(V_i C_i\right)}{\partial t} + \sum_{j=1}^{N_i}\left(g_{ij}\left(p_i - p_j\right)C_{ij} + D_L A_{ij}\frac{C_i - C_j}{l_{ij}}\right) + \sum_{m=1}^{M_i}\left(q_{i,m}C_{i,m} + D_{i,m}A_{i,m}\frac{C_i - C_m}{l_{i,m}}\right) = 0, \tag{3}$$

where V_i is pore volume of pore body i (m^3). C_i is the concentration in pore body i (kg/m^3). C_{ij} is the concentration in pore throat ij (kg/m^3), which is assumed equal to the concentration of the upstream pore body of i and j. $D_L = D_m(1 + \xi Pe^2)$, is the longitudinal dispersion coefficient in pore throat ij (m^2/s), where $D_m = 2.2952 \times 10^{-9}$ is the aqueous molecular diffusion coefficient (m^2/s). $\xi = 0.02083$, is a theoretical parameter for dispersion in a cylindrical tube (Taylor, 1953). $Pe = u_{ij}d_{ij}/(2D_m)$ is the local Peclet number (–), where $u_{ij} = g_{ij}(p_i - p_j)/A_{ij}$ is the fluid velocity in the pore throat (m/s) and $A_{ij} = \pi {\mathrm{d_{ij}}}^2/4$ is the cross-sectional area of the pore throat (m^2). $q_{i,m} = k_{i,m}A_{i,m}\left(p_i - p_m\right)/(\mu_{i,m}l_{i,m})$ is the fluid flux from pore body i to the connected continuum cell m (m^3/s). $D_{i,m}$ is the molecular diffusion coefficient at the interface between pore body i and continuum cell m (m^2/s).

For each continuum microporous cell m, the mass conservation equation is given by

$$\frac{\partial(V_m\phi C)}{\partial t} + \int_{\Omega_m} \nabla \cdot \left(\frac{k\nabla p}{\mu}C + D\nabla C\right) dV + \sum_{i=1}^{W_i}\left(q_{m,i}C_{m,i} + D_{m,i}A_{m,i}\frac{C_m - C_i}{l_{m,i}}\right) = 0, \tag{4}$$

where V_m is the volume of continuum cell (m^3). ϕ is the porosity (–). $D = D_m/\tau$, is the molecular diffusion coefficient in continuum subdomain (m^2/s), where τ is the tortuosity (–). $q_{m,i} = k_{m,i}A_{m,i}\left(p_m - p_i\right)/(\mu_{m,i}l_{m,i})$ is the fluid flux from continuum cell m to pore body i (m^3/s). $D_{m,i}$ is the molecular diffusion coefficient at the interface between continuum cell m and pore body i (m^2/s).

2.2.3. Two-component gas transport in shale

In this section, we present the governing equations for CO_2 and CH_4 in a shale rock sample with two-scale pore structures. The properties of the bulk gas (i.e., a mixture of CH_4 and CO_2) are functions of both pressure and composition (i.e., the mass fractions of CO_2 and CH_4). Because the majority of the pore space in the continuum subdomain of shale rock is on the order of nanometers, we need to account for the interactions between gas molecules and the solid surface (e.g., pore wall) as well as diffusion of the molecules adsorbed at the solid surface in the continuum models. We neglect the adsorption at the solid surfaces and surface diffusion in the resolved pore subdomain due to a relatively small surface area of the pore bodies. For both the pore network and continuum models, we need two governing equations. One for the bulk gas and the other for one of the components. Our model is solved with two primary variables, the pressure of bulk gas (p) and the CO_2 mass fraction (ω^{CO_2}).

The mass balance equations for the bulk gas and CO_2 in a pore body i can be written as

$$V_i \frac{\partial}{\partial t}\left(\rho_i^b\right) + \sum_{j=1}^{N_i} \mathcal{J}_{ij}^b + \sum_{m=1}^{M_i} \mathcal{J}_{i,m}^b = 0 \ , \tag{5}$$

$$V_i \frac{\partial}{\partial t}(\rho_i^b \cdot \omega_i^{CO_2}) + \sum_{j=1}^{N_i} \mathcal{J}_{ij}^{CO_2,adv} + \sum_{j=1}^{N_i} \mathcal{J}_{ij}^{CO_2,diff} + \sum_{m=1}^{M_i} \mathcal{J}_{i,m}^{CO_2} = 0 \ , \tag{6}$$

where the superscript "b" denotes bulk gas (i.e., the mixture of CO_2 or CH_4). The superscripts "adv" and "diff"denote advection and diffusion, respectively. ρ^b is the bulk gas density (kg/m^3). $\mathcal{J}_{ij}^b$ is the mass flux of bulk gas from pore body i to pore body j (kg/s). $\mathcal{J}_{i,m}^b$ is the mass flux of bulk gas from pore body i to continuum cell m (kg/s). ω^{CO_2} is the mass fraction of CO_2 (–). $\mathcal{J}_{ij}^{CO_2,adv}$ is the advective mass flux of CO_2 from pore body i to pore body j (kg/s). $\mathcal{J}_{ij}^{CO_2,diff}$ is the diffusive mass flux of CO_2 from pore body i to pore body j (kg/s). $\mathcal{J}_{i,m}^{CO_2}$ is the mass flux of CO_2 from pore body i to continuum cell m (kg/s).

The density of bulk gas can be expressed as

$$\rho^b = \frac{pM^b}{ZRT}, \tag{7}$$

where p is the pressure of bulk gas (kg/(m $\cdot$ s^2)). $M^b = M^{CO_2}\varpi^{CO_2} + M^{CH_4}\varpi^{CH_4}$ is molar mass of the bulk gas (kg/mol), where M^{CO_2} and M^{CH_4} are molar mass of CH_4 and CO_2, respectively; ϖ^{CO_2} and ϖ^{CH_4} ($\varpi^{CO_2} + \varpi^{CH_4} = 1$ in the system) are the mole fraction of CH_4 and CO_2, respectively. T is temperature (K). R is the ideal gas constant (kg $\cdot$ m^2/(s $\cdot$ K $\cdot$ mol)). $Z = 0.702e^{-2.5T_r}p_r^2 - 5.524e^{-2.5T_r}p_r + 0.044T_r^2 - 0.164T_r + 1.15$ is the compressibility factor (–), where $T_r = T/T_{crt}$ is the reduced temperature (–) and T_{crt} is the critical temperature (K); $p_r = p/p_{crt}$ is the reduced pressure (–) and p_{crt} is the critical pressure (kg/m/s^2) (Mahmoud, 2014).

Here we use a flux model that describes gas flux through cylindrical nanotubes (Beskok & Karniadakis, 1999) to model the flux of the bulk gas through pore throats. The mass flux of the bulk gas and CO_2 can be written as the Hagen-Poiseuille flux q_{H-P} multiplied by a correction factor,

$$\mathcal{J}_{ij}^{b} = f(Kn) g_{ij} \left(p_i - p_j\right) \rho_{ij}^{b}, \tag{8}$$

$$\mathcal{J}_{ij}^{CO_2,adv} = J_{ij}^{b} \cdot \omega_{ij}^{CO_2}, \tag{9}$$

where $f(Kn) = (1 + \alpha Kn)\left(1 + 4Kn/\left(1 + 4Kn\right)\right)$ is the correction factor (–). $\alpha = 2\alpha_0/\left(\pi tan\left(\alpha_1 Kn^{\beta}\right)\right)$, with $\alpha_0 = 64/15\pi$, $\alpha_1 = 4$, and $\beta = 0.4$. $Kn = \lambda/L$ is the Knudsen number (–), where $\lambda = \mu\sqrt{\pi ZRT}/\left(p\sqrt{2M}\right)$ is the mean free path (m), and L is a characteristic length scale for gas flow (m). In the present study, L equals the length of the pore throat ij.

The diffusive mass flux of CO_2 can be expressed as

$$\mathcal{J}_{ij}^{CO_2,diff} = \rho_{ij}^{b} D^{CO_2,diff} A_{ij} \frac{\omega_i^{CO_2} - \omega_j^{CO_2}}{l_{ij}}, \tag{10}$$

where $D^{CO_2,diff}$ is the molecular diffusion coefficient (m^2/s) of CO_2 in the pore throat ij in the resolved pore subdomain.

The mass fluxes of bulk gas and CO_2 between pore body i and continuum cell m are

$$\mathcal{J}_{i,m}^{b} = \frac{k_{i,m} A_{i,m} \left(p_i - p_m\right)}{\mu_{i,m} l_{i,m}} \rho_{ij}^{b}, \tag{11}$$

$$\mathcal{J}_{i,m}^{CO_2} = J_{i,m}^{b} \omega_{i,m}^{CO_2}. \tag{12}$$

In the continuum microporous domain, the mass balance equations in a continuum cell m can be written as

$$\frac{\partial\left(\phi\rho^{b} V_m + \Gamma^{CO_2.ex} V_m + \Gamma^{CH_4.ex} V_m\right)}{\partial t} + \int_{\Omega_m} \nabla \cdot \left(J^{b} + J^{CO_2,sf} + J^{CH_4,sf}\right) dV + \sum_{i=1}^{W_i} J_{m,i}^{b} = 0, \tag{13}$$

$$\frac{\partial(\phi\rho^{b} V_m \cdot \omega^{CO_2} + \Gamma^{CO_2.ex} V_m)}{\partial t} + \int_{\Omega_m} \nabla \cdot \left(J^{CO_2,adv} + J^{CO_2,sf} + J^{CO_2,diff}\right) dV + \sum_{i=1}^{W_i} J_{m,i}^{CO_2} = 0, \tag{14}$$

where the superscript "sf" indicates surface diffusion, and "ex" indicates excess adsorption. $\Gamma^{CO_2,ex}$ is the excess adsorption of CO_2 per unit volume of porous material (kg/m^3). $\rho^{CH_4,ex}$ is the excess adsorption of CH_4 per unit volume of porous material (kg/m^3). $J^{CO_2,sf}$ is the mass flux of CO_2 by surface diffusion ($kg/s/m^2$). $J^{CH_4,sf}$ is the mass flux of CH_4 ($kg/s/m^2$) by surface diffusion. Other variables and parameters have been defined earlier.

Adsorption of CO_2 and CH_4 in shales may be described by the Langmuir isotherm (e.g., Zhang et al., 2012; Heller & Zoback, 2014). For a multicomponent mixture of CO_2 and CH_4, we use the extended two-component Langmuir isotherm to represent the impact of competitive adsorption. Thus, the excess adsorption of CO_2 and CH_4 can be expressed as

$$\Gamma^{CO_2,ex} = \Gamma^{CO_2}_{max} \frac{K^{CO_2} p\varpi^{CO_2}}{1 + K^{CO_2} p\varpi^{CO_2} + K^{CH_4} p\varpi^{CH_4}} \left(1 - \frac{\omega^{CO_2}\rho^b}{\omega^{CO_2,ads} \cdot \rho^{ads}}\right), \tag{15}$$

$$\Gamma^{CH_4,ex} = \Gamma^{CH_4}_{max} \frac{K^{CH_4} p\varpi^{CH_4}}{1 + K^{CO_2} p\varpi^{CO_2} + K^{CH_4} p\varpi^{CH_4}} \left(1 - \frac{\omega^{CH_4}\rho^b}{\omega^{CH_4,ads} \cdot \rho^{ads}}\right), \tag{16}$$

where the superscript "ads" indicates adsorption. $\Gamma^{CO_2}_{max}$, $Gamma^{CH_4}_{max}$ are the maximum adsorption of CO_2 and CH_4 (kg/m^3), respectively. K^{CO_2}, K^{CH_4} is the Langmuir coefficient of CO_2 and CH_4 (m $\cdot$ s^2/kg), respectively. $\omega^{CH_4} = 1 - \omega^{CO_2}$ is the mass fraction of CH_4 (–). $\omega^{CO_2,ads}$ is the mass fraction of CO_2 in the adsorbed phase (–). $\omega^{CH_4,ads}$ is the mass fraction of CH_4 in the adsorbed phase (–). ρ^{ads} is the adsorbed gas density, which is assumed to be constant (1000 kg/m^3).

The mass flux of the bulk gas and CO_2 can be expressed as

$$J^b = -\rho f(Kn) \frac{k}{\mu^b} \nabla p, \tag{17}$$

$$J^{CO_2,adv} = J^b \cdot \omega^{CO_2}, \tag{18}$$

The adsorbed gas can migrate along the pore wall, which causes the surface diffusion process (Ruthven, 1984; Medved and Cerny, 2011). The surface diffusive flux of the bulk gas and CO_2 can be expressed as

$$J^{CO_2,sf} = -\frac{D^{CO_2,sf}}{\tau} \nabla \left(n^{CO_2,ads}\right), \tag{19}$$

$$J^{CH_4,sf} = -\frac{D^{CH_4,sf}}{\tau} \nabla \left(n^{CH_4,ads}\right), \tag{20}$$

where $D^{CO_2,sf}$ is the surface diffusion coefficient of CO_2 (m^2/s).

Similarly, we consider component diffusion in the continuum subdomain. The diffusion flux of CO_2 can be expressed as

$$J^{CO_2,diff} = -\phi\rho^b D^{CO_2,disp} \nabla \omega^{CO_2}, \tag{21}$$

where the superscript "disp" indicates dispersion. $D^{CO_2,disp}$ is the dispersion coefficient of CO_2 (m^2/s).

The interfacial flux of the bulk gas and CO_2 can be expressed as

$$J^b_{m,i} = \frac{k_{m,i} A_{m,i} \left(p_m - p_i\right)}{\mu_{m,i} l_{m,i}}, \tag{22}$$

$$J^{CO_2}_{m,i} = \frac{k_{m,i} A_{m,i} \left(p_m - p_i\right)}{\mu_{m,i} l_{m,i}} \omega^{CO_2} + \phi D^{CO_2,disp} A_{m,i} \frac{\omega_m - \omega_i}{l_{m,i}}, \tag{23}$$

We note that surface diffusion in the interface between pore i and continuum cell m is negligible.

2.3. Numerical methods

We apply a fully implicit numerical framework to solve the mathematical formulations of the h-PNM-continuum models presented in section 2.2. The continuum porous domains are discretized in space using the cell-centered finite volume method. The advection term in the solute transport equations (Eqs. 3 & 4) is discretized using a first-order upwinding scheme. The nonlinear equations resulting from the fully implicit discretization are solved using the Newton-Raphson iteration method. Our implementation of the numerical methods employs the automatic differentiation and gridding utilities in the MATLAB Reservoir Simulation Toolbox (Lie, 2019).

We conduct simulations using existing DNS models implemented in the open-source code OpenFOAM to evaluate the accuracy of the first two mathematical formulations of the hybrid pore network-continuum models. The DNS results for the steady-state single-phase flow are obtained using the simpleFoam solver based on the SIMPLE (Semi-Implicit Method for Pressure Linked Equations) algorithm. The single-phase solute transport DNS results are conducted using the scalarTransportFoam solver.

The initial and boundary conditions for both the h-PNM-continuum and DNS models of each specific test case are presented in sections 3.1–3.3.

3. Results

We conduct numerical experiments to evaluate the h-PNM-continuum modeling framework for each of the mathematical formulations: (1) steady-state single-phase flow, (2) solute transport process, and (3) compositional single-phase flow in shale. The following three subsections present the details of the problem setup and simulation results.

3.1. Steady-state single-phase flow

We simulate steady-state single-phase flow in a 3D digital image of sintered glass beads and compare the simulations to DNS. To analyze the contribution of the continuum subdomain to the flow behavior in the whole domain, we consider two cases: (1) flow in the whole domain including both the resolved pore and the sub-resolution microporous subdomains, and (2) flow only in the resolved pore subdomain.

The physical size of the domain is 0.0025 m $\times$ 0.0025 m $\times$ 0.01 m in x, y, and z with 100 $\times$ 100 $\times$ 400 voxels, respectively. We apply PoreSpy to find all the solid regions within the digital images and then designate one out of every five successively as the continuum microporous region, leading to the continuum subdomain. Subsequent to this step, we employ the procedures outlined in Section 2.1 to extract the pore network and simultaneously couple it to the discretized microporous subdomain. The micropore space in the continuum subdomain relative to the total pore space is 8.8%. The continuum subdomain is assumed to be homogeneous and isotropic with a porosity of $\phi = 0.2$ and a permeability of $k = 3$ Darcy. For both the h-PNM-continuum and DNS models, the porosity of the resolved pore subdomain is 0.278 and the total porosity of the entire domain is 0.304. The fluid is assumed incompressible and is described by Eqs. 1 & 2.

Table 1: Apparent permeability of the whole domain and the resolved pore subdomain from the h-PNM-continuum model and DNS method.

Model	Apparent permeability	
h-PNM-continuum model	k_a^{pore}	6.15×10^{-11}
	k_a	6.61×10^{-11}
DNS method	k_a^{pore}	5.39×10^{-11}
	k_a	5.98×10^{-11}

The initial pressure of the domain is set to 10 Pa. The inlet and outlet boundaries have a fixed pressure of $p_{inlet} = 10$ Pa and of $p_{outlet} = 0$, respectively, imposing a gradient pressure from the inlet to the outlet. The other four faces of the domain are closed and set as no flux boundaries. For the hybrid-PNM-continuum model, an absolute tolerance of 10^{-5} for the numerical residual is used as a convergence criterion for the nonlinear Newton-Raphson iterations. For the DNS, the absolute tolerance is 10^{-10} for the SIMPLE solver.

The overall permeability of the entire domain can be computed using Darcy's law as

$$k_a = \frac{Q\mu L}{A \triangle p} \tag{24}$$

where Q is the volumetric flow rate at the inlet and outlet of the domain (m^3/s) at steady state. $L = L_z$ is the length of the domain along the flow direction (m). $A = L_x \times L_y$ is the cross-sectional area of the domain m^2. $\triangle p = p_{inlet} - p_{outlet}$ is the pressure drop between inlet and outlet.

The computed overall permeability of the entire domain is 6.61×10^{-11} m^2 from the h-PNM-continuum model and 5.98×10^{-11} m^2 from the DNS model (Table 1). The computed permeability of the resolved pore subdomain is 6.15×10^{-11} m^2 and 5.39×10^{-11} m^2 from the PNM and DNS models, respectively. The apparent permeability calculated from the two models is generally in good agreement. Meanwhile, some discrepancies between the two models are observed, which can be primarily attributed to the differences in the resolved pore subdomain. The higher apparent permeability from the h-PNM-continuum model may result from the simplification of the extracted pore network from the digital images by approximating the pore space as cylindrical pore throats and spherical pore bodies. This is a known issue of image-based pore-network modeling. Multiple more advanced approaches have been developed in the literature to improve the accuracy of PNM for image-based pore-scale simulations, including Zhao et al. (2020), and Raeini et al. (2017, 2018). These enhanced PNM approaches can be incorporated into our h-PNM-continuum framework to improve accuracy.

The spatial distributions of pressure from the h-PNM-continuum model and DNS at steady state are presented in Figure 2. The results show that the pressure fields of both the resolved pore subdomain and unresolved microporous subdomain from the h-PNM-continuum model agree well with the DNS results (columns 1 and 2), which further demonstrates the accuracy of the h-PNM-continuum model for simulating steady-state flow.

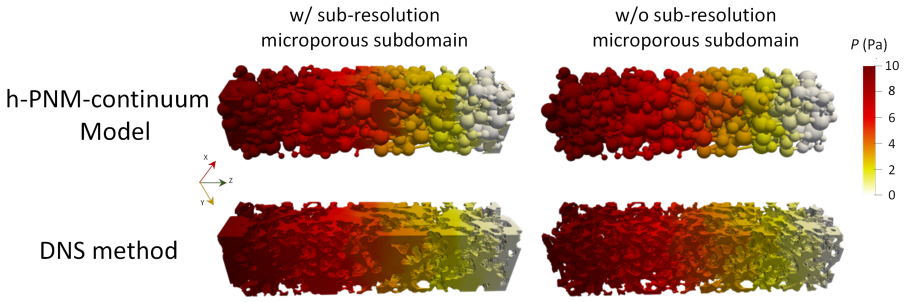

Figure 2: Comparison of pressure distributions in a synthetic porous medium assuming steady-state. Simulations are conducted using the developed h-PNM-continuum model (row 1) versus the DNS method (row 2), with (column 1) versus without (column 2) sub-resolution microporous subdomain.

3.2. Solute transport

We conduct numerical experiments to simulate the transport of a nonreactive solute under steady-state water flow using the same digital pore-scale image from subsection 3.1. To verify the developed model under different flow conditions, we conduct simulations under both low and high Peclet numbers (i.e., $Pe = 0.1$ and 100) and compare the results with that of the DNS method. The Peclet number is defined as

$$Pe = \frac{L_c u}{\phi_e D_m}, \tag{25}$$

where L_c is a characteristic length (m), which is set to L_z. $u = k_a \triangle p/(\mu L_z)$ is the average water flow velocity (m/s). ϕ_e is the effective porosity of the entire domain. D_m is the molecular diffusion coefficient in the resolved pore subdomain and is set to 2.295×10^{-9} m^2/s (which is equal to self-diffusion coefficient of neat water at 25 °C).

The pressure drop between the inlet and the outlet $\triangle p$ is set to 0.1057 Pa and 105.7 Pa to generate the low and high Peclect number scenarios. For solute transport, the initial concentration of the solute is zero. At time $t = 0$, continuous injection of the solute at a concentration of 10 (mol/L) is applied to the inlet. At outlet boundary, the normal gradient of the solute concentration is set to zero.

For convenience, we define a dimensionless time

$$T = \frac{Qt}{\phi_e L_x L_y L_z}, \tag{26}$$

where the definition of Q, ϕ_e, L_x, L_y, and L_z are consistent with above definitions.

In Figure 3, we present the 3D concentration distribution of the entire domain for snapshots in time from two models at low and high Peclet numbers ($Pe = 0.1$ vs. $Pe = 100$). The breakthrough curves (BTCs) of the entire domain for the two Peclet numbers are presented in Figure 4. The spatial concentration distribution and BTCs results show that the h-PNM-continuum model matches well with the DNS model for both the low and high Peclet numbers cases.

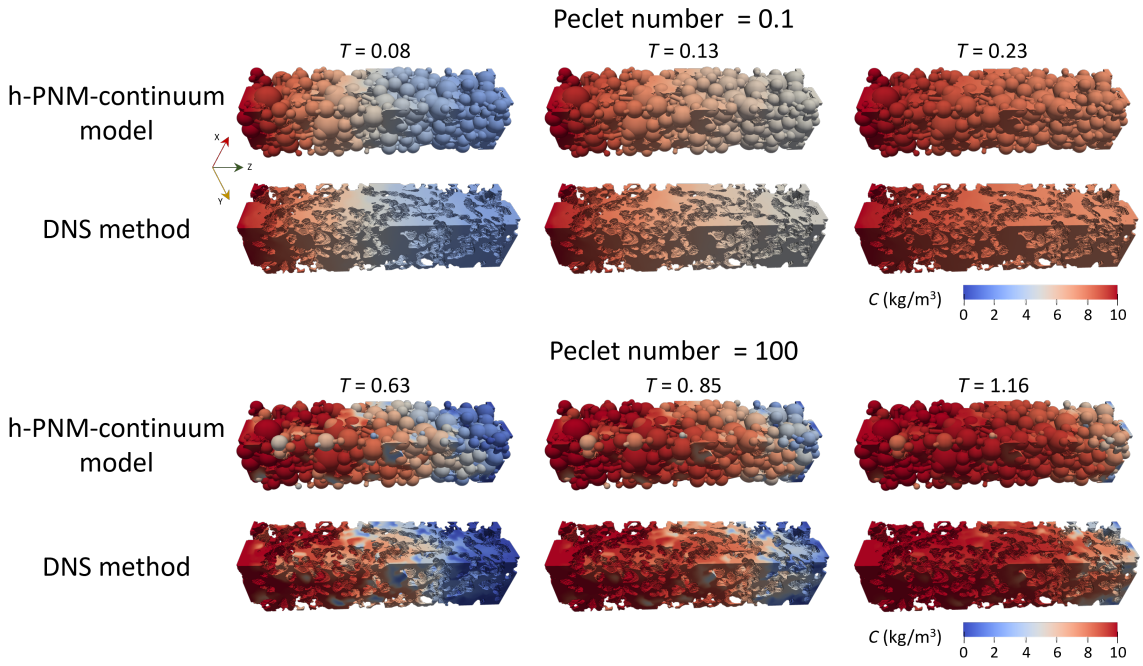

Figure 3: Comparison of the spatial distribution of the solute concentration in the whole domain at $T = 0.08$, 0.13 and 0.23 (column 1, 2, and 3, respectively) for sintered glass beads simulated by the h-PNM-continuum model (rows 1 & 3) and DNS method (rows 2 & 4) at low and high Peclet numbers (i.e., $Pe = 0.1$ and 100, respectively).

For the low Peclet number case, the transport of solute is dominated by diffusion. Under this condition, the assumption of well-mixed solute in each pore body employed by the PNM is reasonable. As a result, excellent agreement between the h-PNM-continuum model and the DNS method is observed for both concentration distribution at different times ($T = 0.08$, 0.13, and 0.23) and the BTCs at the outlet. For the high Peclet number case, advection becomes dominant. From the spatial distribution of the solute concentration, we can see that the plume from the developed h-PNM-continuum model transports slightly faster than the corresponding DNS method. This is because the pore network model assumes a well-mixed condition in each pore body and it has a greater permeability in the resolved pore structure than that computed by the DNS model, both of which lead to faster transport of the solute in the domain. However, even for a high Peclet number regime of Pe=100, the h-PNM-continuum model still appears to provide reliable results compared to direct numerical simulations.

3.3. Compositional single-phase flow

In the third set of numerical experiments, we simulate the injection of CO_2 into a shale sample reconstructed from images obtained using FIB-SEM. The sample is 250 nm $\times$ 250 nm $\times$ 1,000 nm in three dimensions, and the voxel size is 5 nm $\times$ 5 nm $\times$ 5 nm. Voxels in the digital 3D image are segmented into four constituents: resolved pore space, organic matter, clay, and granular minerals. The organic matter and clay regions are represented by the continuum (i.e., the unresolved microporous region), while the granular

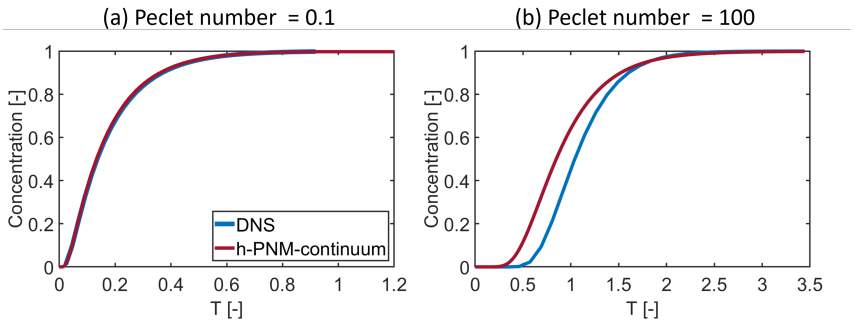

Figure 4: Comparisons of outflow concentration simulated using the developed h-PNM-continuum model (red curves) and the DNS method (blue curves) at low and high Peclet numbers ($Pe = 0.1$ and 100, respectively).

Table 2: Parameters used for the simulations of CO_2 injection into a shale sample.

Parameter	Value
Permeability of the continuum (k)	2 nanoDarcy
Porosity of the continuum (ϕ)	0.1
Langmuir adsorption coefficient for CH_4 (K^{CH_4})	1.7×10^{-7} m $\cdot$ s^2/kg
Langmuir adsorption coefficient for CO_2 (K^{CO_2})	1×10^{-7} m $\cdot$ s^2/kg
Maximum adsorption of CH_4 ($\Gamma^{CH_4}_{max}$)	5 kg/m^3
Maximum adsorption of CO_2 ($\Gamma^{CO_2}_{max}$)	45 kg/m^3
Surface diffusion coefficient for CH_4 ($D^{CH_4,sf}$)	1.14×10^{-8} m^2/s
Surface diffusion coefficient for CO_2 ($D^{CO_2,sf}$)	3.135×10^{-8} m^2/s
Molecular diffusion coefficient of CO_2 in the pore throat ($D^{CO_2,diff}$)	1×10^{-9} m^2/s
Dispersion coefficient of CO_2 in the continuum subdomain ($D^{CO_2,disp}$)	1×10^{-9} m^2/s
Tortuosity (τ)	50

minerals are assumed non-porous solid impermeable to flow. We use the methods described in Section 2.1 to extract and couple the pore network and the continuum grid cells. We simulate two scenarios to examine the contribution of the continuum subdomain to CH_4 production. One considers the entire domain, including the unresolved microporous regions and the other focuses on the resolved pore subdomain only.

For the numerical simulations, the h-PNM-continuum model solves the governing equations described in Section 2.2.3 (Eqs. 5, 6, 13 & 14). We assume that all of the pore space in the shale sample is initially occupied by CH_4 (i.e., $\omega^{CO_2} = 0$) at a gas pressure of 10 MPa and a temperature of 400 K. At the inlet boundary (where $z = 0$), we continuously inject CO_2 (i.e., $\omega^{CO_2} = 1$) at a fixed pressure of 10.1 MPa. At the outlet boundary (where z = 1,000 nm), the pressure is fixed to 10 MPa while the CO_2 mass fraction is set as zero-gradient (i.e., $\partial\omega^{CO_2}/\partial z|_{\text{outlet}} = 0$). Other parameters used in the simulations are presented in Table 2. The Langmuir adsorption coefficients for CH_4 and CO_2, gas diffusion coefficient of CO_2 in the pore throat obtain from (Edwards et al., 2015).

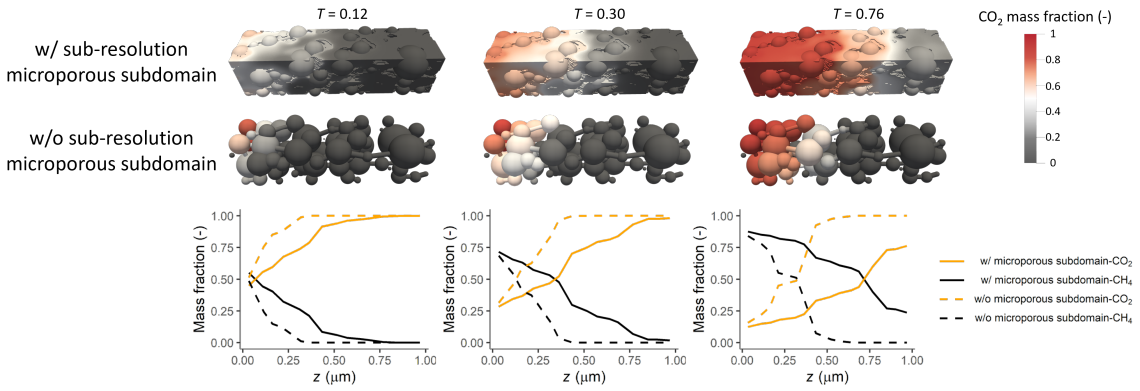

Figure 5: Spatial distributions of CO_2 mass fraction at $T = 0.13$, 0.33 and 0.84 during CO_2 injection simulated with (row 1) and without (row 2) sub-resolution microporous subdomain. Row 3 shows the window-averaged mass fractions along the z axis for CO_2 and CH_4 with and without accounting for the sub-resolution microporous subdomain. Results are simulated using the developed h-PNM-continuum model.

We define a characteristic time scale t_c and use it to define a dimensionless time $T = t/t_c$. t_c is the time when half of the total CH_4 in the entire domain is displaced by CO_2. The spatial distribution of the CO_2 mass fraction and cross-section-averaged mass fraction of CO_2 and CH_4 along the z-direction are presented in Figure 5. The gas pressure in the domain reaches equilibrium relatively quickly (at approximately $T = 0.012$). However, the transport of the CO_2 and CH_4 components lasts much longer. It is interesting that the transport of CO_2 is faster in the presence of the sub-resolution microporous subdomain (Figure 5 (rows 1 & 2)). This is because the microporous subdomain increases the connectivity of the resolved pores, resulting in improved effective connectivity across the entire domain. For real shale rocks, the connectivity of resolved pores is usually limited, while sub-resolution micropores caused by organic matter and clay minerals has the potential of providing storage spaces and migration pathways for hydrocarbon molecules.

The displacement of CH_4 by the injected CO_2 can also be measured by the mass fluxes of the two components at the outlet boundary. In Figure 6(a), the mass rate of CH_4 displaced by CO_2 in the h-PNM-continuum model decreases much faster compared to PNM, which indicates a quick invasion of CO_2 through the whole domain because the improved effective connectivity across the entire domain. Meanwhile, as is shown in Figure 6(b), the cumulative mass production of CH_4 from the whole domain is higher than the resolved pore subdomain. It indicates that the sub-resolution microporous subdomain can continuously serve as a significant source for CH_4 production—the CH_4 production can be as high as 20% of the whole domain. Our modeling results delineate the significant contribution of the continuum subdomain to the overall gas production.

4. Discussion

We have developed a new hybrid pore network-continuum modeling framework (h-PNM-continuum) for simulating flow and transport in 3D multiscale pore structures. Our numerical experiments, spanning from

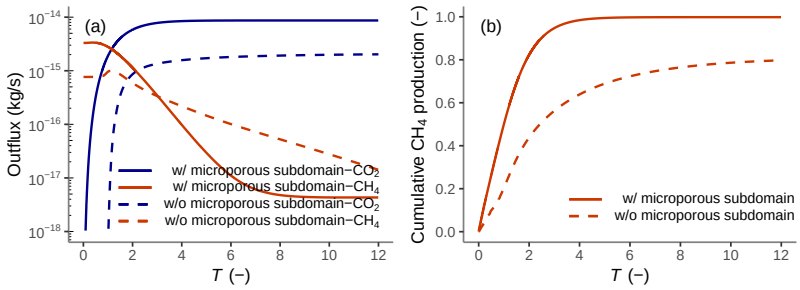

Figure 6: (a) The outflux of CO_2 and CH_4 simulated using the h-PNM-continuum model with and without accounting for the sub-resolution microporous subdomain. (b) Cumulative CH_4 production simulated using the h-PNM-continuum model with and without accounting for the sub-resolution microporous subdomain.

steady-state single-phase flow, single-phase solute transport, and single-phase two-component gas transport, demonstrate that the h-PNM-continuum model can accurately simulate flow and transport processes and the mass transfer between the resolved pore and continuum subdomains, while being much more computationally efficient than the DNS method. Below, we compare the h-PNM-continuum model with other two-scale pore network models, comment on the computational efficiency and numerical accuracy of h-PNM-continuum, and discuss how the h-PNM-continuum modeling framework may be extended to model two-phase flow in 3D multiscale pore structures.

4.1. Comparison with other "two-scale" models

We comment on how our h-PNM-continuum model relates to other "two-scale" network models reported in the literature (Bauer et al., 2012; Jiang et al., 2013; Mehmani & Prodanović, 2014; Bultreys et al., 2015; Prodanović et al., 2015), which we refer to as dual PNMs in the present study. The dual PNMs represent both the resolved pores and the sub-resolution microporous regions of a "two-scale" porous medium. The difference between the different dual PNMs lies in the specific approach for representing the microporous regions and their connectivity with the resolved pore space.

One common approach employed by the dual PNMs is to represent the sub-resolution microporous regions by smaller-scale pore networks. The smaller-scale pore networks can be stochastically generated or based on higher-resolution images that resolve the microporous regions. Jiang et al. (2013) developed a dual PNM, where a small-scale pore network is stochastically generated and then combined with the larger-scale pore network. In their work, (1) two networks (i.e., the large-scale and small-scale networks) were firstly extracted from micro-CT images at different length scales using the Pore Analysis Tools (Jiang et al., 2007; Jiang, 2008). (2) The statistic information from each pore network is used to reconstruct a stochastic network that is representative of the original one (Jiang et al., 2012). (3) Integrating the large-scale and small-scale networks into a single two-scale pore network by connecting the two networks by adding small-scale bonds. For this method, micropores were uniformly distributed in the remaining space that excludes the regions occupied by large-scale network and spatial correlations was not considered. In addition, the coupling of the

two networks was based on a stochastic algorithm rather than the 3D images. Subsequently, Prodanović et al. (2015) proposed another dual PNM where the smaller-scale pore network is constructed from digital images of microporous subdomains. The approach is as follows: (1) First, extracting the large-scale pore network (i.e., macro-network) based on images; (2) Second, identifying the microporous regions in the images; (3) Next, rescaling the small-scale pore network (i.e., micro-network) by a scaling factor to fit into the microporous regions; (4) Lastly, connecting the small-scale network to the larger-scale network to obtain a two-scale network model. A network element generally need not correspond exclusively to a single pore space; rather, it can encapsulate the collective characteristics of a small-scale network within the microporous regions. In terms of dual PNMs proposed by Jiang et al. (2013) and Prodanović et al. (2015), the number of network elements can be a problem for computer simulation since billions of sub-resolution pores are exist even for a small sample.

Another approach that has been used by dual PNMs is to approximate the microporous regions as effective "pore throats" without resolving the pore structures of the microporous regions. Bauer et al. (2012) extracted the resolved pore network (i.e., coarse-scale pore network) from the images and assigned some portion of the resolved pores to be connected by micropores in parallel to resolved pore throats. Bultreys et al. (2015) developed another image-based dual PNM, in which a resolved pore network is extracted from micro-CT images, and micropores are allowed to act both in parallel and in series to the resolved pore network. To determine the connection between micropores and resolved pores, a special link (i.e., micro-link) is added if two pores in the resolved pore network touch the same microporous region, otherwise, the micro-link does not exist or it can be considered as solid. Dual PNMs proposed by Bauer et al. (2012) and Bultreys et al. (2015) although can reduce the computational cost, they could not represent the real structure of micropores, e.g., the location and connection with resolved pores. Even though the connectivity added by the micropores is based on the local micro-CT images, the tortuosity of the connection and geometric details about the microporous region are neglected. Therefore, the main problem of this method is the oversimplified model for the continuum which will result in the underestimation or overestimation of the transport properties (i.e., permeability, porosity) of the whole domain.

Our h-PNM-continuum model treats the micropores as a continuum using models described by the Darcy equation and explicitly represents the flow and transport processes in the resolved pores using a pore network model. In our model, the multiple scales originate directly from flow physics occurring at different scales, i.e., the gas transport in micropores vs. resolved pores. The upscaling is performed to the flow and transport in the micropores, making it a continuum submodel. This approach significantly reduces the computational cost by representing the resolved pore space using PNM and upscaling the micropore space using the continuum-scale model. Additionally, from a numerical perspective, we couple the two submodels using a fully implicit solver, which converges much faster than a domain decomposition method that usually solves the submodels sequentially.

Table 3: Comparison of numerical cells in the developed hybrid pore-network-continuum model and the DNS method.

Model		Synthetic porous medium	Typical shale sample
Resolved pore subdomain	h-PNM-continuum	509	76
	DNS method	1,110,198	153,095
Continuum subdomain	h-PNM-continuum	535,981	345,905
	DNS method		

4.2. Computational efficiency vs. numerical accuracy

The h-PNM-continuum model significantly reduces the computational cost relative to a DNS model. To evaluate the computational efficiency, we compare the number of numerical cells in the two models. The numerical cell numbers for a synthetic porous medium (Sections 3.1 & 3.2) and a shale sample (Section 3.3) are presented in Table 3. The number of numerical cells for the h-PNM-continuum model is over 99.9% smaller than that for the DNS model across all three test cases. While h-PNM-continuum still has a large number of numerical cells for the continuum subdomain (i.e., the same as that of the DNS model), the governing equation there is much simpler relative to that in the resolved pore subdomain for the DNS model. Numerical coarsening strategies may also be developed to reduce the number of numerical cells in the continuum subdomains, given that the flow and transport dynamics are anticipated to be much slower than that in the resolved pore subdomain.

While the h-PNM-continuum is much more computationally efficient than the DNS model, the approximation of representing the resolved pore space by a pore network introduces additional errors just like any other pore network models. In the present study, we employ a basic version of PNM to demonstrate the image-based hybrid framework for coupling a PNM with a continuum scale model. More advanced PNMs reported in the literature have significantly improved their predictive capabilities (Mehmani & Tchelepi, 2017; Raeini et al., 2017, 2018; Zhao et al., 2020). As discussed in Section 3.1, These enhanced PNM approaches can be incorporated into our h-PNM-continuum framework to further improve the accuracy.

4.3. Extension of the hybrid framework for other applications

In addition to the examples demonstrated in the present study, the h-PNM-continuum modeling framework can also be potentially generalized to model more complex processes in two-scale porous media, such as two-phase flow or reactive transport. Extending the h-PNM-continuum to model two-phase flow in two-scale porous media can be particularly attractive given that they are computationally expensive when simulated by DNS models. Here, we outline the conceptual steps for extending the h-PNM-continuum model for modeling two-phase flow in a two-scale porous medium. For the resolve pore subdomain, we may employ a dynamic PNM or a quasi-static PNM to represent the two-phase flow, depending on the question of interest. For instance, for the two-scale porous media where there is a significant contrast between the pore sizes of the resolve pore subdomain and the sub-resolution continuum subdomain, the two-phase flow in the resolved

pore subdomain is expected to be much slower than that in the microporous region. In this case, it may be sufficient to use a quasi-static PNM for the resolved pore subdomain. The quasi-static distribution of the two fluid phases can be updated based on the fluxes at the interfaces between the resolved pore subdomain and the continuum domain. For the continuum subdomain, we can employ the standard two-phase flow model at the continuum scale. The two-phase flow properties of the microporous region (i.e., capillary pressure as a function of phase saturation and relative permeability function) may be estimated from higher-resolution images or pore-size distribution information (e.g., obtained by mercury intrusion or nitrogen adsorption).

5. Conclusion

We have developed an image-based hybrid pore network-continuum (h-PNM-continuum) modeling framework for the flow and transport processes in two-scale porous media. The hybrid framework treats the unresolved microporous region as a continuum and models the flow and transport at the Darcy scale, while explicitly representing the flow and transport processes in the larger pores through a computationally efficient pore network model. The h-PNM-continuum modeling framework couples the pore network with the microporous subdomain based on the original connectivity between the two subdomains from 3D digital images.

We validate the modeling framework by comparing it to DNS methods in a set of numerical experiments including steady-state incompressible single-phase flow and solute transport. The results suggest that the h-PNM-continuum model can accurately predict the overall flow and transport process and the mass transfer between the resolved pores and the sub-resolution microporous subdomains, while being much more computationally efficient than the DNS methods. We demonstrate the applicability of the hybrid model for simulating two-component gas transport in shale rocks using the displacement of CH_4 by CO_2 as an example. The simulations illustrate the significant contribution of the continuum subdomain to the overall gas production. While the present study focuses on single-phase flow and transport, the h-PNM-continuum modeling framework may also be further extended to simulate more complex processes that involve multiphase flow, reactive transport, and non-Newtonian displacement. If desired, more advanced PNM approaches can also be incorporated into the h-PNM-continuum modeling framework to further improve the accuracy of representing flow and transport processes in the resolved pore subdomain.

List of variables

Name	**Definition**
Subscript i or j	Pore body labeled i or j.
Subscript m	The grid cells in the continuum microporous subdomain that are connected to pore body i.
Subscript ij	Pore throat ij that connects pore bodies i and j.

Name	**Definition**
Subscript i, m	The connection between pore body i and the connected continuum cell m.
Subscript m, i	The connection between the connected continuum cell m and pore body i.
Superscript b	Bulk gas (i.e., the mixture of CO_2 or CH_4).
Superscript ads	Adsorption.
Superscript ex	Excess adsorption.
Superscript adv	Advection.
Superscript $diff$	Diffusion.
Superscript $disp$	Dispersion.
Superscript sf	Surface diffusion.
A_{ij}	The cross-sectional area of the pore throat (m^2).
$A_{i,m}$	Area of the interface (m^2).
$A_{m,i}$	Area of the interface (m^2).
C_i	Concentration in pore body i (kg/m^3).
C_{ij}	The concentration in pore throat ij (kg/m^3).
D	The molecular diffusion coefficient in continuum subdomain (m^2/s).
$D^{CH_4,sf}$	Surface diffusion coefficient of CH_4 (m^2/s).
$D^{CO_2,diff}$	The molecular diffusion coefficient of CO_2 in the pore throat ij (m^2/s).
$D^{CO_2,disp}$	The dispersion coefficient of CO_2 in the continuum subdomain (m^2/s).
$D^{CO_2,sf}$	Surface diffusion coefficient of CO_2 (m^2/s).
$D_{i,m}$	The molecular diffusion coefficient at the interface between pore body i and continuum cell m (m^2/s).
$D_{m,i}$	The molecular diffusion coefficient at the interface between continuum cell m and pore body i (m^2/s).
D_L	The longitudinal dispersion coefficient in pore throat ij (m^2/s).
D_m	Aqueous molecular diffusion coefficient (m^2/s).
d_{ij}	Diameter of the pore throat ij (m).
ϕ	Porosity (–).
$f(Kn)$	The correction factor (–).
$\Gamma^{CH_4,ex}$	Excess adsorption of CH_4 per unit volume of porous material (kg/m^3).
$\Gamma^{CO_2,ex}$	Excess adsorption of CO_2 per unit volume of porous material (kg/m^3).
$\Gamma^{CH_4}_{max}$	Maximum adsorption of CH_4 (kg/m^3).
$\Gamma^{CO_2}_{max}$	Maximum adsorption of CO_2 (kg/m^3).
g_{ij}	The conductance between pore bodies i and j ($m^4 \cdot s/kg$).
$\mathcal{J}^b_{ij}$	Mass flux of bulk gas from pore body i to pore body j (kg/s).
$\mathcal{J}^b_{i,m}$	Mass flux of bulk gas from pore body i to continuum cell m (kg/s).

Name	Definition
$\mathcal{J}_{ij}^{CO_2,adv}$	Advective mass flux of CO_2 from pore body i to pore body j (kg/s).
$\mathcal{J}_{ij}^{CO_2,diff}$	Diffusive mass flux of CO_2 from pore body i to pore body j (kg/s).
$\mathcal{J}_{i,m}^{CO_2}$	Mass flux of CO_2 from pore body i to continuum cell m (kg/s).
$J^{CH_4,sf}$	Mass flux of CH_4 by surface diffusion (kg/s/m^2).
$J^{CO_2,sf}$	Mass flux of CO_2 by surface diffusion (kg/s/m^2).
K^{CH_4}	The Langmuir coefficient of CH_4 (m $\cdot$ s^2/kg).
K^{CO_2}	The Langmuir coefficient of CO_2 (m $\cdot$ s^2/kg).
k	Permeability of cell m (m^2).
λ	The mean free path (m).
L	A characteristic length scale for gas flow (m).
l_{ij}	Length of the pore throat ij (m).
$l_{i,m}$	Distance from pore body i to continuum cell m (m).
$l_{m,i}$	Distance from continuum cell m to pore body i (m).
μ	Fluid viscosity (kg/m/s).
M_i	Number of continuum cells connected to pore body i (–).
M^b	Molar mass of the bulk gas (kg/mol).
M^{CH_4}	Molar mass of CH_4.
M^{CO_2}	Molar mass of CO_2.
N_i	Number of pore bodies connected to pore body i (–).
Ω_m	The domain of integration.
ω^{CH_4}	Mass fraction of CH_4 (–).
ω^{CO_2}	Mass fraction of CO_2 (–).
$\omega^{CH_4,ads}$	Mass fraction of CH_4 in the adsorbed phase (–).
$\omega^{CO_2,ads}$	Mass fraction of CO_2 in the adsorbed phase (–).
p	Pressure in pore bodies or continuum microporous cells (kg/m/s^2).
Pe	Local Peclet number (–).
p_r	The reduced pressure (–).
p_{crt}	The critical pressure (kg/m/s^2).
ϖ^{CO_2}	Mole fraction of CO_2.
ϖ^{CH_4}	Mole fraction of CH_4.
$q_{i,m}$	The volumetric flux between pore body i and continuum cell m (m^3/s).
$q_{m,i}$	The volumetric flux between continuum cell m and pore body i (m^3/s).
ρ^{ads}	Adsorbed gas density kg/m^3).
ρ^b	Bulk gas density (kg/m^3).
R	The ideal gas constant (kg $\cdot$ m^2/(s $\cdot$ K $\cdot$ mol)).

Name	Definition
τ	Tortuosity (–).
T	Temperature (K).
T_r	The reduced temperature (–).
T_{crt}	The critical temperature (K).
V_m	Volume of continuum cell (m^3).
V_i	Pore volume of pore body i (m^3).
W_i	Number of pore bodies connected to continuum cell m (–).
ξ	A theoretical parameter for dispersion in a cylindrical tube.
Z	The compressibility factor (–).

Acknowledgment

This work was supported by the Strategic Priority Research Program of the Chinese Academy of Sciences (XDB10010501). Acknowledgment is made to the donors of the American Chemical Society Petroleum Research Fund for partial support of this research to B. Guo (62523-DNI9).

References

Bauer, D., Youssef, S., Fleury, M., Bekri, S., Rosenberg, E., & Vizika, O. (2012). Improving the estimations of petrophysical transport behavior of carbonate rocks using a dual pore network approach combined with computed microtomography. *Transport in porous media*, *94*, 505–524.

Bekri, S., Laroche, C., & Vizika, O. (2005). Pore network models to calculate transport and electrical properties of single or dual-porosity rocks. In *SCA* (p. 2005). volume 35.

Beskok, A., & Karniadakis, G. E. (1999). Report: a model for flows in channels, pipes, and ducts at micro and nano scales. *Microscale thermophysical engineering*, *3*, 43–77.

Blunt, M. J., Bijeljic, B., Dong, H., Gharbi, O., Iglauer, S., Mostaghimi, P., Paluszny, A., & Pentland, C. (2013). Pore-scale imaging and modelling. *Advances in Water resources*, *51*, 197–216.

Bultreys, T., De Boever, W., & Cnudde, V. (2016). Imaging and image-based fluid transport modeling at the pore scale in geological materials: A practical introduction to the current state-of-the-art. *Earth-Science Reviews*, *155*, 93–128.

Bultreys, T., Van Hoorebeke, L., & Cnudde, V. (2015). Multi-scale, micro-computed tomography-based pore network models to simulate drainage in heterogeneous rocks. *Advances in Water resources*, *78*, 36–49.

Carrillo, F. J., & Bourg, I. C. (2019). A darcy-brinkman-biot approach to modeling the hydrology and mechanics of porous media containing macropores and deformable microporous regions. *Water Resources Research*, *55*, 8096–8121.

Carrillo, F. J., & Bourg, I. C. (2021). Modeling multiphase flow within and around deformable porous materials: A darcy-brinkman-biot approach. *Water Resources Research*, *57*, e2020WR028734.

Carrillo, F. J., Bourg, I. C., & Soulaine, C. (2020). Multiphase flow modeling in multiscale porous media: An open-source micro-continuum approach. *Journal of Computational Physics: X*, *8*, 100073.

Carrillo, F. J., Soulaine, C., & Bourg, I. C. (2022). The impact of sub-resolution porosity on numerical simulations of multiphase flow. *Advances in Water Resources*, *161*, 104094.

Cnudde, V., & Boone, M. N. (2013). High-resolution x-ray computed tomography in geosciences: A review of the current technology and applications. *Earth-Science Reviews*, *123*, 1–17.

Edwards, R. W., Celia, M. A., Bandilla, K. W., Doster, F., & Kanno, C. M. (2015). A model to estimate carbon dioxide injectivity and storage capacity for geological sequestration in shale gas wells. *Environmental science & technology*, *49*, 9222–9229.

Golfier, F., Zarcone, C., Bazin, B., Lenormand, R., Lasseux, D., & Quintard, M. (2002). On the ability of a darcy-scale model to capture wormhole formation during the dissolution of a porous medium. *Journal of fluid Mechanics*, *457*, 213–254.

Gostick, J. T. (2017). Versatile and efficient pore network extraction method using marker-based watershed segmentation. *Physical Review E*, *96*, 023307.

Guo, B., Ma, L., & Tchelepi, H. A. (2018). Image-based micro-continuum model for gas flow in organic-rich shale rock. *Advances in Water Resources*, *122*, 70–84.

Guo, B., Mehmani, Y., & Tchelepi, H. A. (2019). Multiscale formulation of pore-scale compressible darcy-stokes flow. *Journal of Computational Physics*, *397*, 108849.

Heller, R., & Zoback, M. (2014). Adsorption of methane and carbon dioxide on gas shale and pure mineral samples. *Journal of unconventional oil and gas resources*, *8*, 14–24.

Jiang, Z. (2008). *Quantitative characterisation of the geometry and topology of pore space in 3D rock images*. Ph.D. thesis Heriot-Watt University.

Jiang, Z., Van Dijke, M., Sorbie, K. S., & Couples, G. D. (2013). Representation of multiscale heterogeneity via multiscale pore networks. *Water resources research*, *49*, 5437–5449.

Jiang, Z., Van Dijke, M., Wu, K., Couples, G. D., Sorbie, K. S., & Ma, J. (2012). Stochastic pore network generation from 3d rock images. *Transport in porous media*, *94*, 571–593.

Jiang, Z., Wu, K., Couples, G., Van Dijke, M. I. J., Sorbie, K. S., & Ma, J. (2007). Efficient extraction of networks from three-dimensional porous media. *Water resources research*, *43*.

Lie, K.-A. (2019). *An introduction to reservoir simulation using MATLAB/GNU Octave: User guide for the MATLAB Reservoir Simulation Toolbox (MRST)*. Cambridge University Press.

Maes, J., & Menke, H. P. (2021). Geochemfoam: Direct modelling of multiphase reactive transport in real pore geometries with equilibrium reactions. *Transport in Porous Media*, *139*, 271–299.

Maes, J., & Menke, H. P. (2022). Geochemfoam: Direct modelling of flow and heat transfer in micro-ct images of porous media. *Heat and Mass Transfer*, *58*, 1937–1947.

Maes, J., Soulaine, C., & Menke, H. P. (2022). Improved volume-of-solid formulations for micro-continuum simulation of mineral dissolution at the pore-scale. *Frontiers in Earth Science*, *10*, 917931.

Mahmoud, M. (2014). Development of a new correlation of gas compressibility factor (z-factor) for high pressure gas reservoirs. *Journal of Energy Resources Technology*, *136*.

Meakin, P., & Tartakovsky, A. M. (2009). Modeling and simulation of pore-scale multiphase fluid flow and reactive transport in fractured and porous media. *Reviews of Geophysics*, *47*.

Mehmani, A., & Prodanović, M. (2014). The effect of microporosity on transport properties in porous media. *Advances in Water Resources*, *63*, 104–119.

Mehmani, Y., Anderson, T., Wang, Y., Aryana, S. A., Battiato, I., Tchelepi, H. A., & Kovscek, A. R. (2021). Striving to translate shale physics across ten orders of magnitude: What have we learned? *Earth-Science Reviews*, *223*, 103848.

Mehmani, Y., & Tchelepi, H. A. (2017). Minimum requirements for predictive pore-network modeling of solute transport in micromodels. *Advances in water resources*, *108*, 83–98.

Molins, S., Soulaine, C., Prasianakis, N. I., Abbasi, A., Poncet, P., Ladd, A. J., Starchenko, V., Roman, S., Trebotich, D., Tchelepi, H. A. et al. (2021). Simulation of mineral dissolution at the pore scale with evolving fluid-solid interfaces: Review of approaches and benchmark problem set. *Computational Geosciences*, *25*, 1285–1318.

Prodanović, M., Mehmani, A., & Sheppard, A. P. (2015). Imaged-based multiscale network modelling of microporosity in carbonates. *Geological Society, London, Special Publications*, *406*, 95–113.

Rabbani, A., Jamshidi, S., & Salehi, S. (2014). An automated simple algorithm for realistic pore network extraction from micro-tomography images. *Journal of Petroleum Science and Engineering*, *123*, 164–171.

Raeini, A. Q., Bijeljic, B., & Blunt, M. J. (2017). Generalized network modeling: Network extraction as a coarse-scale discretization of the void space of porous media. *Physical Review E*, *96*, 013312.

Raeini, A. Q., Bijeljic, B., & Blunt, M. J. (2018). Generalized network modeling of capillary-dominated two-phase flow. *Physical Review E*, *97*, 023308.

Scheibe, T. D., Perkins, W. A., Richmond, M. C., McKinley, M. I., Romero-Gomez, P. D., Oostrom, M., Wietsma, T. W., Serkowski, J. A., & Zachara, J. M. (2015). Pore-scale and multiscale numerical simulation of flow and transport in a laboratory-scale column. *Water Resources Research*, *51*, 1023–1035.

Soulaine, C., Creux, P., & Tchelepi, H. A. (2019). Micro-continuum framework for pore-scale multiphase fluid transport in shale formations. *Transport in Porous Media*, *127*, 85–112.

Soulaine, C., Gjetvaj, F., Garing, C., Roman, S., Russian, A., Gouze, P., & Tchelepi, H. A. (2016). The impact of sub-resolution porosity of x-ray microtomography images on the permeability. *Transport in porous media*, *113*, 227–243.

Soulaine, C., Roman, S., Kovscek, A., & Tchelepi, H. A. (2017). Mineral dissolution and wormholing from a pore-scale perspective. *Journal of Fluid Mechanics*, *827*, 457–483.

Soulaine, C., Roman, S., Kovscek, A., & Tchelepi, H. A. (2018). Pore-scale modelling of multiphase reactive flow: application to mineral dissolution with production of CO_2. *Journal of Fluid Mechanics*, *855*, 616–645.

Soulaine, C., & Tchelepi, H. A. (2016). Micro-continuum approach for pore-scale simulation of subsurface processes. *Transport in Porous Media*, *113*, 431–456.

Taylor, G. I. (1953). Dispersion of soluble matter in solvent flowing slowly through a tube. *Proceedings of the Royal Society of London. Series A. Mathematical and Physical Sciences*, *219*, 186–203.

Wildenschild, D., & Sheppard, A. P. (2013). X-ray imaging and analysis techniques for quantifying pore-scale structure and processes in subsurface porous medium systems. *Advances in Water resources*, *51*, 217–246.

Xiong, Q., Baychev, T. G., & Jivkov, A. P. (2016). Review of pore network modelling of porous media: Experimental characterisations, network constructions and applications to reactive transport. *Journal of contaminant hydrology*, *192*, 101–117.

Xu, Q., Dai, X., Yang, J., Liu, Z., & Shi, L. (2022). Image-based modelling of coke combustion in a multiscale porous medium using a micro-continuum framework. *Journal of Fluid Mechanics*, *932*, A51.

You, J., & Lee, K. J. (2021). Analyzing the dynamics of mineral dissolution during acid fracturing by pore-scale modeling of acid-rock interaction. *SPE Journal*, *26*, 639–652.

Zhang, T., Ellis, G. S., Ruppel, S. C., Milliken, K., & Yang, R. (2012). Effect of organic-matter type and thermal maturity on methane adsorption in shale-gas systems. *Organic geochemistry*, *47*, 120–131.

Zhao, J., Qin, F., Derome, D., & Carmeliet, J. (2020). Simulation of quasi-static drainage displacement in porous media on pore-scale: Coupling lattice boltzmann method and pore network model. *Journal of Hydrology*, *588*, 125080.